

Design of a Lamb-shift polarimeter for pulsed intense polarized H^+/D^+ ion sources*

Yaojie Zhai,^{1,2} Sheng Zhang,^{1,2} Boxing Gou,^{1,2} Xuezhen Zhang,¹ Yuguo Liu,¹ Qianyu Jin,^{1,2,†} and Liangting Sun^{1,2,‡}

¹*Institute of Modern Physics, Chinese Academy of Sciences, Lanzhou 730000, China*

²*School of Nuclear Science and Technology, University of Chinese Academy of Sciences, Beijing 100049, China*

An intense spin polarized H^+/D^+ ion source (SPIS) based on the principle of atomic beam source and resonant plasma ionizer is under development at Institute of Modern Physics (IMP, CAS) for the future Electron-ion collider in China (EicC). In order to measure the polarization of the pulsed H^+/D^+ beam extracted from the SPIS at an energy of 25 keV, a Lamb-shift polarimeter (LSP) has been designed. Compared with the polarization measurement utilizing nuclear reactions that demands polarized ion beam accelerated to the MeV level, LSP operated at a low energy is evidently more convenient. Moreover, thanks to its principle, LSP can function normally even in the presence of a mixed H_2^+ component in the extracted polarized D^+ beam, which is inevitable for the polarized ion source utilizing resonant plasma ionizer. An ion beam transport system aiming at modifying the beam spin orientation and decelerating the beam from 25 keV to 2.5 keV is incorporated into the LSP, which enables the LSP to be used directly at downstream of the SPIS. In this work, all of the involved critical physical processes and components of the LSP have been modeled, analyzed and designed carefully to ensure high efficiency at each stage of its operation. Even for a low duty factor pulsed ion beam, the LSP is capable of measuring the polarization with a precision of 1 % in a few seconds.

Keywords: Spin polarization, Polarized ion source, Lamb-shift polarimeter

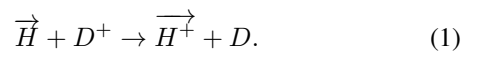
I. INTRODUCTION

The electron-ion collider has been recognized as an ideal tool to explore the inner structure and interactions of the nucleons and nuclei. The Electron-ion collider in China (EicC) has been proposed and is under conceptual design phase [1, 2]. The EicC is suggested to be built by upgrading the High Intensity heavy-ion Accelerator Facility (HIAF) which is currently under construction [3, 4]. The featured physics at EicC includes the emergence of the proton spin and mass, the nucleon partonic structure, exotic hadron states, *etc.* To pursue such scientific goals, EicC is conceptually designed to deliver high luminosity collisions involving highly polarized electron, proton and light ions [5–7]. Therefore, it is essential for the EicC to achieve production, acceleration and preservation of polarized ion and electron beams. Some research and development (R&D) projects such as key technologies prototyping have already been initiated to support these objectives. [8]. As one of the R&D projects for EicC, a spin polarized ion source (SPIS) to produce intense H^+/D^+ beams with high polarization is under development at Institute of Modern Physics (IMP, CAS).

Technologies of polarized ion source have undergone significant development since the 1960s, culminating in considerable progress to the present day. Modern polarized ion sources generate polarized ion beams with intensity of mA level and polarization of about 80 %. In polarized ion sources, the process always involves the generation of atoms with po-

larized nuclei followed by ionization to produce polarized ions. At present, atomic beam-type and optically pumped polarized ion sources (ABPIS and OPPIS), classified by polarized atom generation, are mainly used to provide polarized ion beam to accelerator. There are different ionization schemes available for ABPIS and OPPIS to produce positive or negative polarized ions. Performances of several typical polarized ion sources are listed in table 1. Status of polarized ion sources development has been reviewed in refs. [9, 10].

The SPIS developed at IMP is based on the principle of atomic beam source and resonant plasma ionizer. It is designed to produce polarized H^+/D^+ ion beam of 1 mA, 25 keV, with pulse width of 100 μ s, repetition frequency of 5 Hz and polarization of no less than 80 %. The layout of the SPIS is shown in Fig. 1. The hydrogen molecules are injected into a dissociator (1) through a pulsed solenoid valve (15) and are dissociated into atoms with a radio-frequency (RF) discharge. The flow out channel of the dissociator is wrapped by a cold copper clip (2) which is cooled to 70 K by a refrigerator (3), so that the velocity dispersion of the atoms is reduced. The atomic beam is collimated by a skimmer (4). Two permanent sextupole magnets (5 and 7) and three RF transition units (6, 8, and 9) are used to polarize the atomic beam. By switching on specific sets of RF transition units, beams of desired polarization modes can be produced. The polarized H atoms and D^+ ions from deuterium plasma jet produced by an arc plasma source (14) are injected toward each other and intersect in a storage cell (13) where polarized protons are formed through the quasi-resonant charge exchange reactions [16],



To avoid depolarization during the charge exchange, the storage cell is placed in a solenoid magnet (12), which generates a magnetic field of about 0.3 T, much stronger than the critical field of the ground state hydrogen (deuterium) atom ($B_{c,H}^{1S} = 50.7$ mT, $B_{c,D}^{1S} = 11.7$ mT) [17]. Both, the polar-

* Supported by the National Key Research and Development Program of China (No. 2020YFE0202004, 2023YFA1606801), the National Natural Science Foundation of China (No.12375162) and the Natural Science Foundation of Gansu Province, China (No. 24JRRA039).

† Corresponding author, Qianyu Jin, Nanchang Road 509, Lanzhou, Gansu Province, PRC, jinqianyu@impcas.ac.cn.

‡ Corresponding author, Liangting Sun, Nanchang Road 509, Lanzhou, Gansu Province, PRC, sunlt@impcas.ac.cn.

Table 1. Performances of several typical polarized ion sources.

Year	Institute	Particle	Intensity	Duty Factor	Polarization	Polarization Acquisition	Ionizer
2007	INR, RAS [11]	H^+, H^-	11 mA, 4 mA	200 μ s, 10 Hz	90%	ABPIS	Plasma Ionizer
2014	BNL [10]	H^-	4 mA	300 μ s, 1 Hz	85%	OPPIS	Na Jet
2007	FZJ [12]	H^-	50 μ A	20 ms, 0.5 Hz	90%	ABPIS	Cs Beam
2018	JINR [13]	D^+	6 mA	150 μ s, 1 Hz	88%	ABPIS	Plasma Ionizer
2002	IUCF [14]	H^-, D^-	1.8 mA, 2 mA	300 μ s, 3 Hz	90%	ABPIS	Plasma Ionizer
2023	BNL [15]	$^3He^{++}$	Goal: 2 mA	20 μ s	70%	OPPIS	EBIS*

*Electron Beam Ion Source.

ized protons and the unpolarized deuterons are pulled out by a beam extraction system (11), and are spatially separated by a bending magnet (10). Their currents are measured by a Faraday cup (17) or a beam dump (16), respectively. Then the beam polarization is measured by a Lamb-shift polarimeter (18) assembled downstream the SPIS. When the SPIS is operated for a polarized deuteron beam, the inlet gas of the atomic beam source and of the plasma ionizer are switched. However, it is inevitable that the extracted polarized D^+ beam will be mixed with an unpolarized H_2^+ component since the D^+ and H_2^+ ions can't be separated by the bending magnet. Not until the beam is pre-accelerated can the H_2^+ ions be stripped into protons and then be swept out [13].

Beam polarization is one of the main quantities characterizing a polarized ion beam. For proton (spin-1/2) beams produced by an axially symmetric polarized ion source, it is sufficient to describe the polarization with the vector polarization,

$$P_z = n_+ - n_-, \quad (2)$$

where n_{\pm} are the occupation numbers of protons with spin parallel and antiparallel to the quantization axis along z . For deuteron (spin-1) beams the tensor polarization,

$$P_{zz} = 1 - 3n_0, \quad (3)$$

is required in addition to fully describe their polarization states. Here n_0 is the occupation number of deuterons with spin perpendicular to z .

It is necessary to measure the beam polarization quickly and accurately downstream the SPIS for precise investigation of the spin depolarization in the subsequent acceleration, even for the operation of the SPIS. Utilizing suitable nuclear reactions with known and adequate analyzing power and cross section, beam polarization can be determined by the angular asymmetry of the reaction products. However, at the beam energy of 25 keV, there are hardly any competent nuclear reactions. Unless, the beam is pre-accelerated before the polarization measurement [13, 18]. In this way, expensive accelerator time has to be used for optimizing and tuning the SPIS. Lamb-shift polarimeter (LSP) based on the atomic processes sensitive to the nuclear spin polarization is more preferred in the vicinity of several keV [19, 20]. Moreover, LSP can function normally despite the mixed H_2^+ component within the extracted polarized D^+ beam from the plasma ionizer. Therefore, a LSP is under intense development at IMP for measuring the polarization of the beam produced by the SPIS.

II. PRINCIPLES OF LAMB-SHIFT POLARIMETER

Spin filter is the core component of LSP. It was originally invented for the Lamb-shift polarized ion source (LSPIS) at Los Alamos National Laboratory (LANL) in the late 1960's [21]. Spin filter consists of a solenoid magnet providing an uniform magnetic field B_s parallel to the beam, and a cylindrical RF resonant cavity providing a longitudinal RF electric field E_{rf} , a transversal RF magnetic B_{rf} and a transversal static electric field E_s . Installed inside and coaxially with respect to the solenoid, the RF resonant cavity works in the mode of TM_{010} with a frequency of 1610 MHz. It is divided into two pairs of opposing quadruplets. One pair is used for radio frequency (RF) power coupling and signal pick-up, and to the other a DC voltage is applied symmetrically. Spin filter utilizes a three-level resonance interaction among the $n = 2$ hyperfine states of the hydrogen (deuterium) atom, which was first reported in 1951 by Lamb and Rutherford [22]. Hydrogen (deuterium) atoms in the 2S state are metastable with a lifetime of 1/7 s. Atoms in the 2P state undergo an allowed electric-dipole decay with a lifetime of 1.6 ns. Fig. 2 shows the $2S_{1/2}$ and $2P_{1/2}$ levels of the hydrogen atom in an external magnetic field with nuclear hyperfine structure included. The levels are labeled with α , β , e and f , based on the nomenclature first introduced by Lamb and Rutherford [23]. The notation $|m_j, m_I\rangle$ indicates the spin projections of electron and proton in a strong magnetic field. The energies of states α and e (with electron spin parallel to the magnetic field, $m_j = 1/2$) increase with the magnetic field, while that of β and f ($m_j = -1/2$) decrease. In the region around 57.5 mT, the β and e levels cross each other and the splitting between states α and β (e) is about 1610 MHz. The transversal electric field E_s mixes states β and e , while the longitudinal RF electric field E_{rf} mixes α and e , which lead the lifetime of the metastable α and β to decrease sharply. In general, all metastable atoms in this region will be quenched into the ground state before they exit the spin filter. Exceptions occur when the α - β resonance is induced by the transversal RF magnetic field B_{rf} , which reduces the α - e resonance, allowing about 50 % of the atoms in α state to survive. Note that the width of the α - e resonance is approximately 7 mT depending on the lifetime of state e , whereas that of the α - β resonance is only about 0.5 mT. In other words, superposition of the α - β resonance on the α - e resonance, i.e., the α - β - e three-level resonance interaction, makes it possible for atoms in α states to pass through spin filter without quenching. The three-level resonance is so sharp that it can be ob-

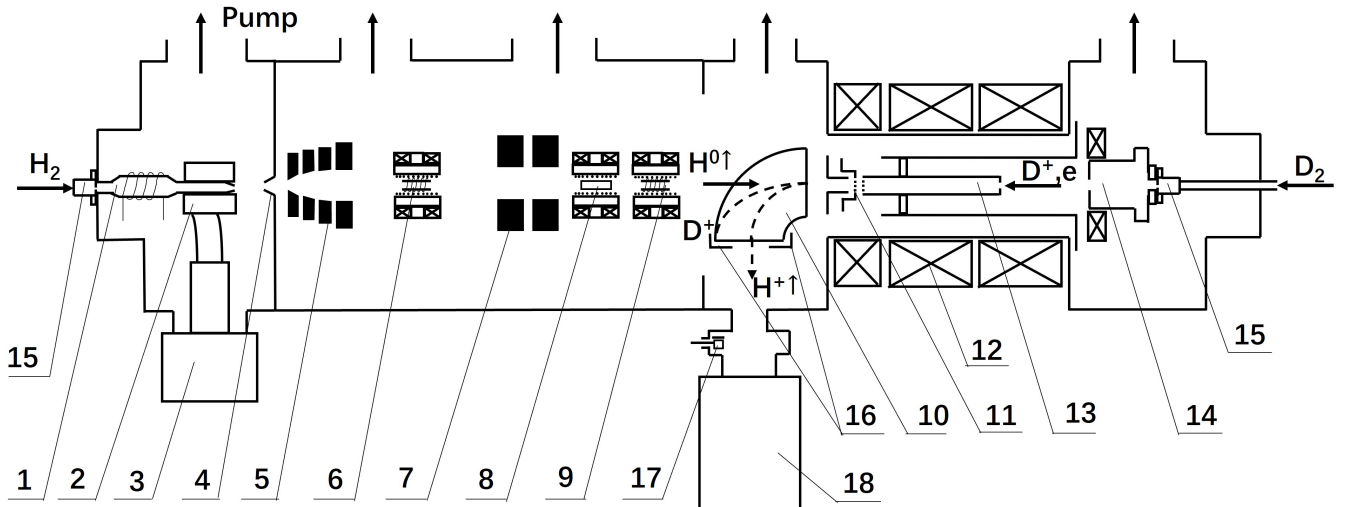


Fig. 1. Layout of the SPIS. (1) Dissociator, (2) cold copper clip, (3) refrigerator, (4) skimmer, (5 and 7) permanent sextupole magnet, (6) medium field RF transition unit, (8) strong field RF transition unit, (9) weak field RF transition unit, (10) bending magnet, (11) beam extraction system, (12) solenoid, (13) storage cell, (14) arc plasma source, (15) solenoid valve, (16) beam dump, (17) Faraday cup, (18) Lamb-shift polarimeter.

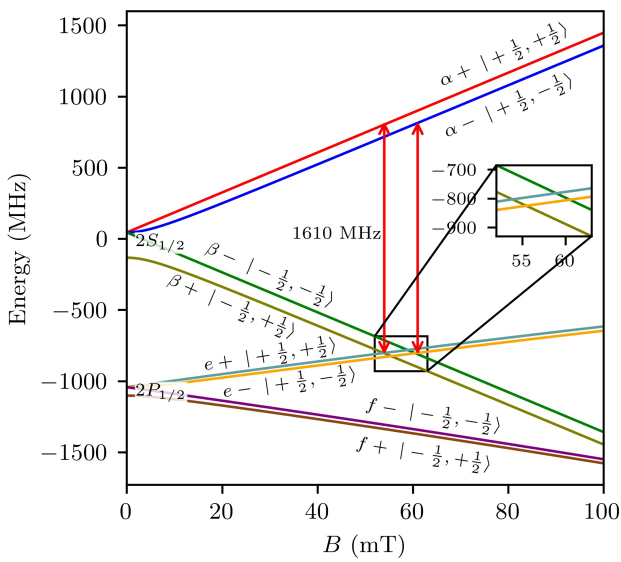


Fig. 2. The $2S_{1/2}$ and $2P_{1/2}$ levels of the hydrogen atom in an external magnetic field with nuclear hyperfine structure included.

served for each hyperfine state. As shown in the enlargement of Fig. 2, there are two resonances for hydrogen at 54.0 and 61.0 mT, corresponding to $m_I = \pm 1/2$, respectively. For deuterium, the resonances are at 56.4, 57.4, and 58.4 mT, corresponding to $m_I = +1, 0, -1$, respectively. With the B_s in the resonant values, all the metastable atoms are quenched within spin filter except ones in the resonant m_I state due to the three-level resonance. That is to say, spin filter can pick out the metastable atoms with a specific m_I by varying the magnetic field B_s .

The layout of the LSP at IMP is shown in Fig. 3. For making it feasible for the polarized H^+/D^+ beams extracted from the SPIS, an ion beam transport aiming at modifying the spin orientation and the energy of the beam is incorporated into the LSP, including an Einzel lens, a Wien filter and a deceleration lens. The polarized proton beam extracted from the SPIS is focused by the Einzel lens into the Wien filter, where spin orientations of the protons are rotated to the beam direction. In the deceleration lens the beam is decelerated from 25 keV to 2.5 keV/u to guarantee enough dwell time of the metastable atoms in the spin filter, which is the pre-condition for the spin filter to work properly [24]. After the deceleration lens, a portion of the protons are converted into metastable hydrogen atoms through charge exchange as they pass through a sodium oven, where a strong magnetic field is employed to prevent depolarization. Subsequently, a spin filter is utilized to quench all metastable atoms except ones with the selected m_I , depending on the magnetic field B_s of the spin filter. The residual metastable atoms are quenched later by a quenching lens, and the Lyman- α photons (121 nm), emitted by the transitions, are registered by a photomultiplier tube (PMT). As the metastable atoms with different m_I are selected in the spin filter, the number of photons counted by the PMT is proportional to the metastable atoms with the selected m_I , which in turn is proportional to the number of protons with the selected m_I in the primary ion beam. The beam polarization is determined directly. When the LSP is used to measure the deuteron beam polarization, the mixed H_2^+ ions also can be converted into metastable atoms at the sodium oven and the corresponding resonances will appear in the spin filter. But these resonances are clearly separated due to the distant resonance values of the magnetic field B_s . The polarization of the deuteron beam polarization can be measured without being affected. Because the beam produced by

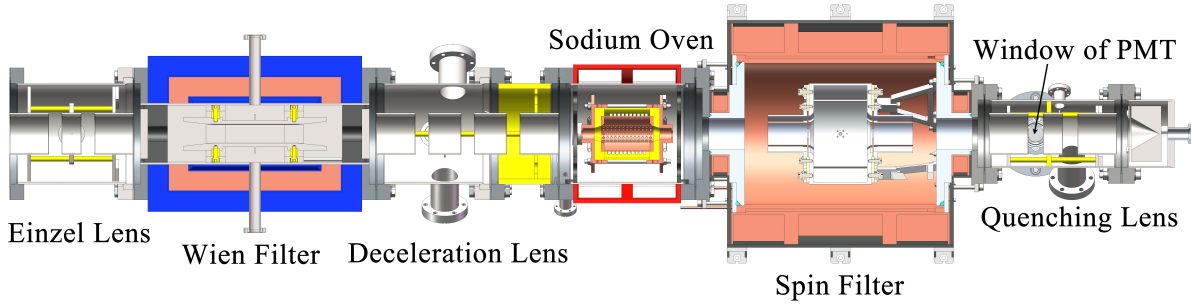


Fig. 3. Layout of the LSP at IMP.

197 the SPIS is pulsed, with an averaged intensity of $0.5 \mu\text{A}$, in
198 order to get adequate statistical precision as soon as possible,
199 each component of the LSP is designed carefully to ensure
200 high efficiency throughout every stage of the measurement
201 process [25].

210 The red arrows in Fig. 4 represent the spin orientations of
211 the polarized protons (deuterons). The original spin orienta-
212 tion $\vec{S}_{H/D}^i$ is determined by the magnetic field of the ioniza-
213 tion region. After being bent by the dipole magnet, not only
214 the beam direction is changed, but also the spin orientation.
215 According to the Larmor precession equation,

$$216 \quad \frac{d\vec{S}}{dt} = \vec{\mu} \times \vec{B} = g \frac{q}{2m} \vec{S} \times \vec{B}, \quad (4)$$

202 **III. ION BEAM TRANSPORT**
203 The ion beam transport line, shown in Fig. 4, is located be-
204 tween the ionizer and the sodium oven. As mentioned above,
205 it modifies both the energy (velocity) and the spin orientation
206 of the ion beam. Simultaneously, it is optimized to maximize
207 the number of ions entering the acceptance of the downstream
208 sodium oven and the spin filter, which enables higher statistic
209 precision to be achieved in a shorter time.

217 where \vec{S} is the spin angular momentum, and $\vec{\mu}$, g , q , m the
218 magnetic moment, g -factor ($g_p = 5.586$, $g_D = 1.714$), elec-
219 tric charge and ion mass of the particle, respectively. There-
220 fore, \vec{S} precesses around the opposite direction of the mag-
221 netic field with an angular frequency,

$$222 \quad \omega_L = \frac{g}{2} \frac{q}{m} B_{\perp}, \quad (5)$$

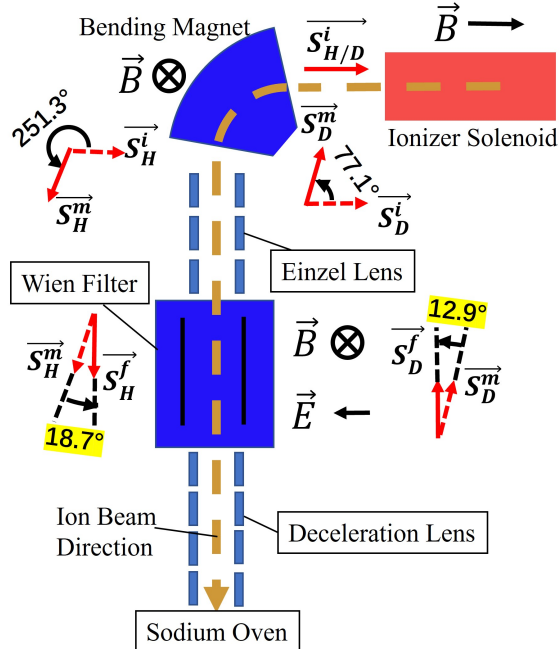


Fig. 4. Layout of the ion beam transport.

223 where B_{\perp} is the component of the magnetic field perpendic-
224 ular to \vec{S} . Supposing that the effective length of the magnetic
225 field is L and the particle's speed is v , the precession angle of
226 \vec{S} can be written as,

$$227 \quad \phi = \omega_L \frac{L}{v} = \frac{g}{2} \frac{q}{mv} B_{\perp} L = \frac{g}{2} \frac{B_{\perp} L}{[B\rho]}, \quad (6)$$

228 where the relativity is ignored and $[B\rho]$ represents the particle
229 magnetic rigidity. From Eq. (6) it is easy to obtain that if the
230 dipole magnetic field deflects the ion beam by an angle of θ ,
231 the spin orientation will precess around the opposite direction
232 of the dipole magnetic field by an angle of $g\theta/2$. As depicted
233 in Fig. 4, after being bent by the dipole magnet, the spin ori-
234 entation is rotated from $\vec{S}_{H/D}^i$ to $\vec{S}_{H/D}^m$. Based on the same
235 principle, the Wien filter is used to rotate the spin of proton
236 (deuteron) by a well-defined angle, from $\vec{S}_{H/D}^m$ to $\vec{S}_{H/D}^f$, to
237 make it parallel (antiparallel) to the beam direction.

238 Space charge effect during the low energy (25 keV) and
239 high-current ion beam transport is inevitable [26]. Based on
240 the quasi-resonant charge exchange ionization scheme, it is
241 estimated that the extraction of a 1 mA polarized proton beam
242 is accompanied by an unpolarized deuteron beam of about

243 50 mA [27]. Although the unpolarized deuterons can be sep-
 244 arated out in the bending magnet, and almost all of the space
 245 charge effect in the bending magnet can be compensated by
 246 the electrons produced through collisions between ions and
 247 the residual gas molecules or beam loss at the vacuum cham-
 248 ber wall [28, 29]. In the subsequent electrostatic elements,
 249 there is almost no compensation for the space charge, as the
 250 neutralization electrons are rapidly repelled by the electric
 251 fields. For polarized deuteron beam the space charge effect
 252 is more serious, because they are always accompanied by un-
 253 separated H_2^+ ions.

254 To determine the optimal configuration of the ion beam
 255 transport line, a beam transport simulation was conducted. In
 256 the simulation, the beam was considered to be a direct current
 257 (DC) rather than a pulse. Fig. 5 shows the calculated evolu-
 258 tion of the double rms envelop of deuteron beam of 6 mA
 259 (equivalent to D^+ and accompanied H_2^+ in intensity of 1 mA
 260 and 5 mA, respectively) and of 25 keV from the exit of the
 261 ion beam extraction system to the quenching gap faced by the
 262 PMT window. At the exit of the ion beam extraction system,
 263 the beam is cylindrically symmetric in KV distributions in
 264 vertical and horizontal directions and the initial Twiss param-
 265 eters are set as follows:

$$\alpha_{x,y} = 0, \beta_{x,y} = 0.169 \pi \text{mm mrad}^{-1}, \\ \epsilon_{norm,rms,x,y} = 0.375 \pi \text{mm mrad},$$

266 adopting the result from previous experiments with a simi-
 267 lar devices [27]. After the exit of the ion beam extraction
 268 system, there is a drift section of 100 mm before the dipole
 269 magnet. The dipole magnet bends the beam by 90° with
 270 a radius of 100 mm and provides focus force in both ver-
 271 tical and horizontal directions with a pair of inclined pole
 272 faces and a field decline indicator of 0.5 [30]. Subsequently,
 273 the beam drifts 425 mm reaching the entrance of the Einzel
 274 lens. The ion beam transport in this section is calculated by
 275 TraceWin code [31]. The three-dimensional magnetic field of
 276 the dipole magnet calculated by OPERA [32] is imported and
 277 the space charge effect is ignored. After the dipole magnet,
 278 the deuteron beam passes through the Einzel lens, the Wien
 279 filter, the deceleration lens and arrives at the sodium oven. At
 280 the middle plane of the sodium oven, the deuterons are as-
 281 sumed to be converted to metastable atoms. Following, the
 282 atoms drift through the spin filter and reach the quenching
 283 chamber. Simulation for the beam transport in this section
 284 was finished by IBSimu code [33]. Space charge effects are
 285 accounted for through multiple iterations. Particle trajec-
 286 tories are initially calculated without considering space charge.
 287 Subsequently, the corresponding space charge is incorporated
 288 based on the previously calculated trajectories, and this pro-
 289 cess is repeated until the solution converged to the required
 290 precision. The ion beam transport through each element is
 291 simulated sequentially, with the beam phase space distribu-
 292 tion from the end of the last element being used as the initial
 293 condition for the next element. The transmission efficiency
 294 of the ion beam transport is defined as the ratio of the num-
 295 ber of the particles arriving at the quenching gap to the initial
 296 number of the particles at the exit of the beam extraction sys-
 297 tem. According to the simulation, the transmission efficiency

298 of the deuteron beam can be optimized to 4 %. For the proton
 299 beam, the maximum transmission reaches 8 %.

301 IV. SODIUM OVEN

302 In the sodium oven, a portion of protons (deuterons) is con-
 303 verted to metastable atoms through charge-exchange. The
 304 sodium oven is shown schematically in Fig. 6. To avoid de-
 305 polarization, the sodium oven is installed in a solenoid pro-
 306 ducing a magnetic field of up to 70 mT, which is stronger
 307 than the critical field of the metastable hydrogen (deuterium)
 308 atom ($B_{c,H}^{2S} = 6.3 \text{ mT}$, $B_{c,D}^{2S} = 1.5 \text{ mT}$) [17]. Metal sodium
 309 is loaded into a reservoir made of copper. As the reservoir
 310 is heated by a coil heater, sodium vapor emerges into a cell
 311 channel through openings on it. Two end plates with a central
 312 hole of 10 mm limit the sodium vapor flowing into the neigh-
 313 boring elements. Between the end plate and the reservoir,
 314 thermal insulation material (ZrO_2) is employed. Addition-
 315 ally, cooling water has been added to the two end plates. In
 316 this way, the temperature of the two end plates is always be-
 317 low the melting point of sodium (98°C), which is conducive
 318 to reduce the sodium vapor diffusion into the neighboring el-
 319 ements.

320 For protons (deuterons) of 2.5 keV/u, the cross section of
 321 charge exchange for metastable atom production is about $1 \times$
 $322 10^{-15} \text{ cm}^2$ [34, 35]. The metastable atom yield depends on
 323 the thickness of the sodium target Π . According to the result
 324 of the previous experiments, the optimal target thickness Π
 325 should be $2 \times 10^{14} \text{ cm}^{-2}$, and the maximum yield is about
 326 0.1 [36, 37]. With a thinner target, it is more likely that the
 327 protons will pass through the target without colliding with
 328 the sodium atoms. However, with a thicker target, multiple
 329 collisions may occur before the protons exit, leading to the
 330 collisionally deexcitation of the metastable atoms.

331 The target thickness Π depends on the reservoir tempera-
 332 ture. To determine a suitable reservoir temperature for achiev-
 333 ing the optimal target thickness Π , the evaporation of sodium
 334 has been simulated using the Molecular Flow Module of
 335 COMSOL [38–40]. In the simulation, the bottom of the reser-
 336 voir is set as an evaporation surface. The evaporation rate, i.e.,
 337 the number of sodium atoms evaporated from the surface per
 338 unit area per unit time, is determined by the surface tempera-
 339 ture as

$$340 Q = \alpha \sqrt{\frac{N_A^2}{2\pi M RT}} P_s(T), \quad (7)$$

341 where N_A is the Avogadro's number, $M = 23 \text{ g/mol}$ is the
 342 Molar mass of sodium, $R = 8.314 \text{ J K}^{-1} \text{ mol}^{-1}$ is the gas
 343 constant, $T [\text{K}]$ is the temperature of the evaporation face, α
 344 is the evaporation coefficient, and the $P_s(T)$ is the saturated
 345 vapor pressure of the sodium as a function of the temperature
 346 $T [\text{K}]$. The dependence of the P_s on the temperature is given
 347 by [41],

$$348 \lg P_s [\text{mmHg}] = -\frac{5567}{T [\text{K}]} - 0.5 \lg T [\text{K}] + 9.235. \quad (8)$$

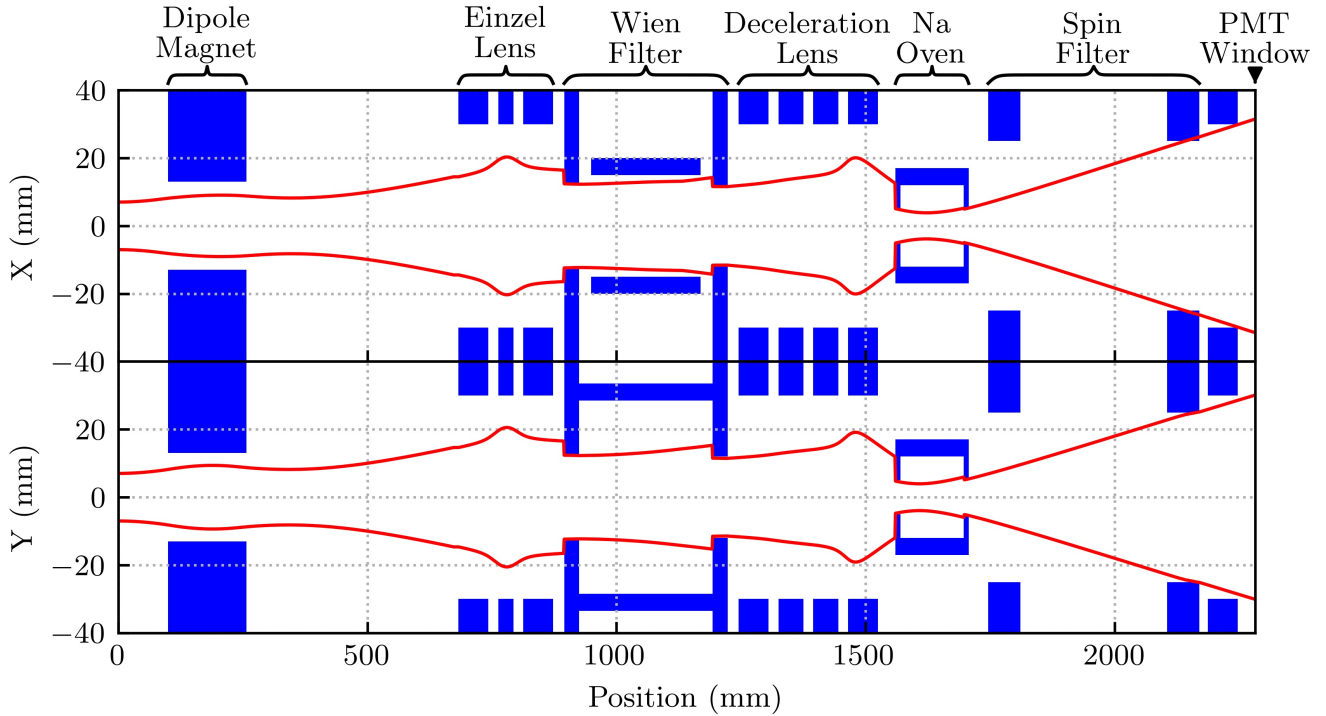


Fig. 5. The simulated double rms envelop of the deuteron beam of 6 mA and of 25 keV from the exit of the ion beam extraction system to the quenching gap faced by the PMT window. After being bent by the dipole magnet, the beam is focused by the Einzel lens, of which the middle electrode is on a potential of 15 kV. Then, at the Wien filter the beam spin orientation is rotated by an angle of 12.9° by its magnetic field. And the potential of the two plate electrodes of the Wien filter are ± 780 V, respectively. Following, in the deceleration lens the beam is decelerated from 25 keV to 5 keV. The potentials of the four cylinder electrodes are 0, 2, 1 and 20 kV, respectively. It is noticeable that all of the downstream elements behind the deceleration lens are floated at a potential of 20 kV. Subsequently, the deuterons are converted to metastable atoms at the sodium oven and drift to the quenching gap.

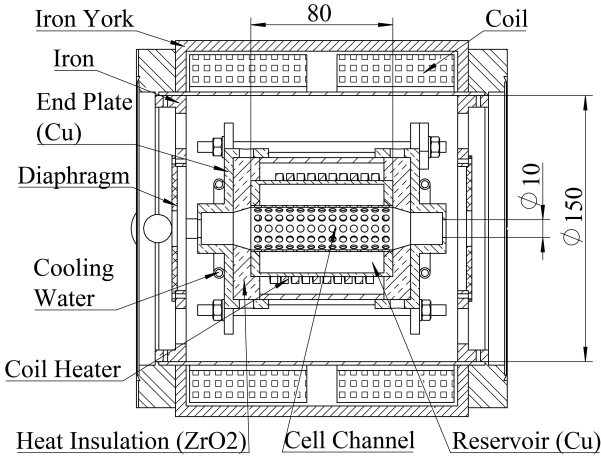
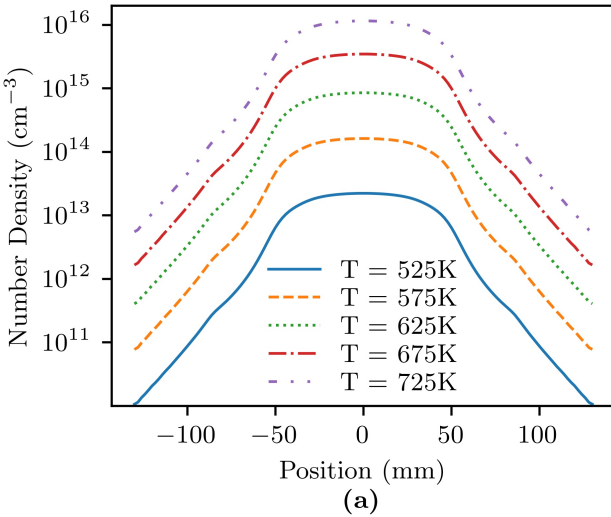


Fig. 6. Cross-sectional view of the sodium oven.

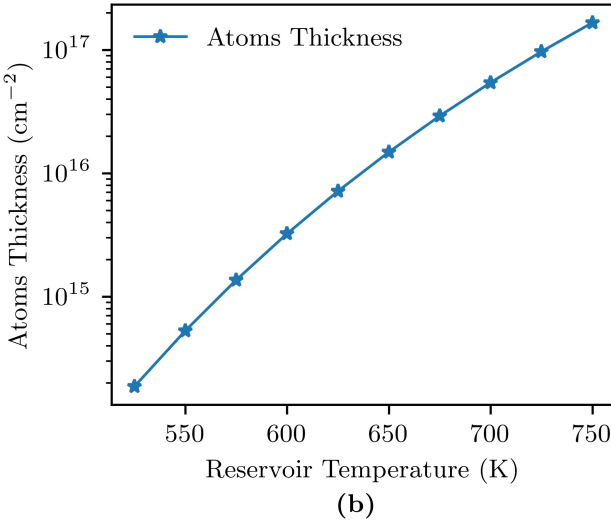
It is assumed that the sodium atoms are backscattered when they collide with the interior walls of the reservoir, while they will be absorbed when they collide with the other faces of the oven due to the low temperature of these faces. Fig. 7 (a) shows the simulated number density distribution of the

sodium atoms along the axis of the oven for different reservoir temperatures. Outside the cell channel (-40 to 40 mm) the number density of sodium atoms decreases rapidly. The integration of the atom number density along the axis, i.e., the atoms thickness, is shown in Fig. 7 (b) as a function of the reservoir temperature. At 525 K, the sodium atoms thickness is about 2×10^{14} cm $^{-2}$, a suitable value for production of the metastable atoms, and the average pressure of the reservoir is about 0.2 Pa. The actual operation temperature of the reservoir should be higher than 525 K, because the evaporation coefficient is set to the ideal value 1 in the simulation.

A steady-state thermal analysis of the sodium oven has been done with ANSYS [42]. The thermal conductivity of copper and ZrO₂ are set to 400 and 2 W m $^{-1}$ K $^{-1}$, respectively. The loop of cooling water on the end plate is designed carefully. At the inlet, the water speed and temperature are specified to 1.5 m/s and 20 °C, respectively. At the outlet, the water pressure is set to 0 Pa. When the coil heater power is 300 W, the simulated steady-state temperature distribution is shown in Fig. 8. With a temperature of the reservoir of 250 °C, the periphery of the sodium oven keeps a significantly lower temperature. According to further simulations, even with more heater power and reservoir temperature, such as 450 °C, the periphery of the sodium oven is less than



(a)



(b)

Fig. 7. The simulated number density distribution of the sodium atoms along the axis of the oven (a) and the target thickness (b) for different reservoir temperatures.

378 50 °C.

379

V. SPIN FILTER

380 The spin filter is shown schematically in Fig. 9. Its consists
 381 of a solenoid magnet and a RF resonant cavity. Because spin
 382 filter is based on the three-level resonance interaction, inade-
 383 quate homogeneity of the static magnetic field (B_s) provided
 384 by the solenoid magnet can cause unexpected quenching of
 385 the metastable atoms. A successful spin filter applied for the
 386 polarimeter requires an axial magnetic field uniform to ± 0.05
 387 mT over the central region of the spin-filter cavity [43]. The
 388 solenoid magnet comprises of five windings (C1, B1, A, B2
 389 and C2), wound around copper skeletons. The system of the
 390 windings has been optimized with OPERA [32]. As shown
 391 by the insert of Fig. 10, the fluctuation of the solenoid mag-

C: Steady-State Thermal

Figure 2
 Type: Temperature
 Unit: °C
 Time: 1 s

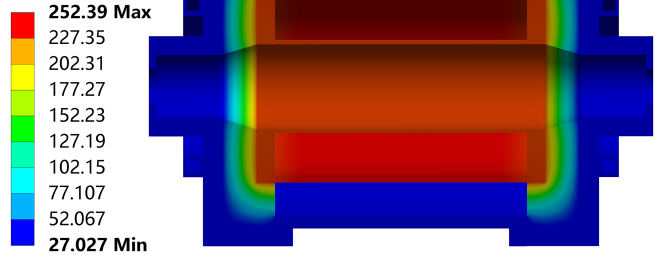


Fig. 8. The temperature distribution with a sectional view of the sodium oven from a steady state simulation with 300 W of heating power applied on the outside surface of the reservoir.

392 netic field is less than ± 0.02 mT at 60 mT over the central
 393 region of the spin filter cavity. To shield the interference with
 394 the magnetic field uniformity caused by external fields, espe-
 395 cially the fringe field from the upstream sodium oven, all of
 396 the windings are enclosed by iron yokes. In addition, to avoid
 397 the frequency shift of the RF resonant cavity led by thermal
 398 expansion, an interlayer for water cooling is designed in the
 399 copper skeleton, which effectively prevents the heat transfer
 400 from the windings to the cavity. It should be noted that the
 401 magnetic field in the spin filter must be parallel to the field in
 402 the sodium oven. Otherwise, unwanted Sona transitions may
 403 take place in the zero-crossing region, which will distort the
 404 polarization measurement results [44].

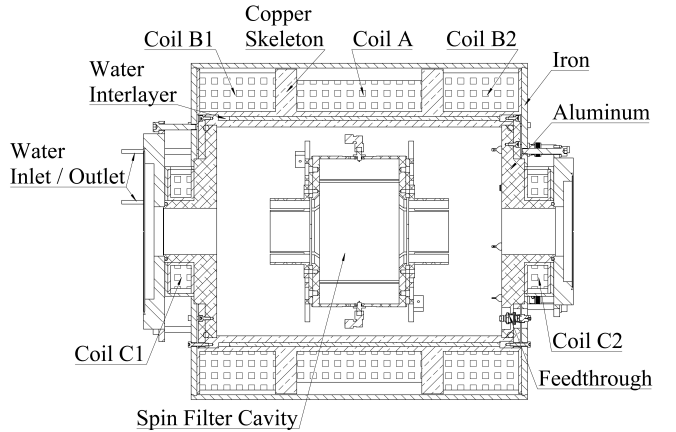


Fig. 9. Cross-sectional view of the spin filter.

405 The RF resonant cavity is a cylindrical cavity with a length
 406 of 82 mm and a radius of 75 mm. Each end of the cavity
 407 is fitted with an end pipe that has a smaller radius of 30 mm.
 408 The cavity is split into four sectors. One pair of opposing sec-
 409 tors are grounded and serves the purpose of RF feeding and
 410 sampling. The other two sectors are applied with symmet-
 411 ric voltages, which are used to generate a transversal electric
 412 field inside the cavity. The slots between these sectors can be

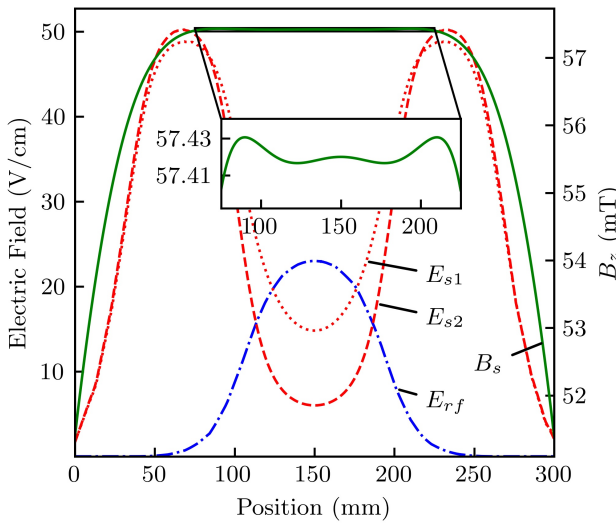


Fig. 10. The spin filter magnetic and electric fields distribution.

manipulated to fine-tune the cavity's resonance frequency to 1610 MHz. Fig. 10 illustrates the simulated distribution of the longitudinal RF electric field with a dash-dotted (E_{rf}) line. Similarly, the two end pipes also are divided into four sectors. The sectors adjacent to the RF feeding and sampling sectors of the cavity are grounded, while the other two are floated and can be applied with symmetric voltages. This setup allows for the static electric field within the cavity and the end pipes to be altered independently. As shown by the dotted (E_{s1}) and dashed (E_{s2}) lines in Fig. 10, besides the transversal static electric field of 10–20 V/cm inside the cavity, an enhanced field of about 50 V/cm is established in the end pipes. This stronger field is designed to deflect protons (deuterons) that fail to capture an electron in the sodium oven. The deflection is essential, because the protons (deuterons) can reach the downstream quenching chamber. Their arrival induces a non-linear background signal in the PMT, which fluctuates with the magnetic field of the spin filter. This variability makes the signal processing challenging.

An effective spin filter should possess two key characteristics. First, it should exhibit a high transmission for metastable atoms in the resonant m_I states, facilitating the acquisition of high statistical precision in a shorter measurement time. Second, a good spin filter must demonstrate a high selectivity for metastable atoms with different m_I values, which is a fundamental requirement for accurate beam polarization measurement. Both, the transmission and the selectivity, are depending on various influencing factors, including the velocity of the metastable atoms, uniformity of the axial static magnetic field, and distributions of the static electric fields and the RF fields. While there are established general principles derived from prior calculations and experiments, an effective spin filter design entails a quantitative and comprehensive evaluation of the transmission and the selectivity under various spin filter design parameters.

The calculation can be conducted by employing a time-

dependent quantum mechanical approach to analyze the atomic four-level system, α , β , e and f levels, as was done in the refs. [45, 46]. The spin filter operates in a magnetic field (50–60 mT) much stronger than the critical magnetic field B_c of hydrogen (deuterium) atom in 2S and 2P states. Therefore, the quantum number m_I is conserved and each group of the four atomic levels associated with the same m_I can be individually considered. The perturbed Schrödinger equation may be written as,

$$(\hat{H}_0 + \hat{H}') \psi = i\hbar \frac{\partial \psi}{\partial t}, \quad (9)$$

where H_0 is a Hamiltonian including the influence of an ideal uniform static magnetic field, whose eigenfunctions satisfy the equation $H_0 u_0 = E_n u_n$, and H' symbolize perturbations of the RF fields, the static electric field and the fluctuated static magnetic field. Expanding the atomic wave function ψ with u_n ,

$$\psi = \sum_n a_n(t) u_n e^{-iE_n t/\hbar}, \quad (10)$$

the coefficients $a_k(t)$ satisfy the differential equations,

$$i\hbar \dot{a}_k = \sum_n H'_{kn} a_n e^{i\omega_{kn} t}, \quad (11)$$

where

$$\begin{aligned} \omega_{kn} &= (E_k - E_n)/\hbar, \\ H'_{kn} &= \int u_k^* \hat{H}' u_n dt. \end{aligned}$$

The perturbation matrix elements H'_{kn} can be calculated and are given in ref. [46]. Damping terms accounting for the spontaneous decay of the e and f states also can be included in Eq. 11. A Python code has been written to calculate the time-evolution of the individual α , β , e and f state amplitudes, denoted as a , b , c and d by numerical integration of the Eq. 11.

As a metastable α -state deuterium atom with $m_I = 0$ going through the spin filter with an energy of 2.5 keV/u, time-evolutions of $|a|^2$ and $|a|^2 + |b|^2$ for three different fields configurations are shown in the left plot of Fig. 11. Case ① has a uniform electrostatic field of 15 V/cm, the realistic RF electric field and static magnetic field as shown respectively by the dash-dotted (E_{rf}) and solid (B_s) curves in Fig. 10. In case ② and ③, replace the uniform electrostatic field with the real one as shown by the dotted (E_{s1}) and dashed (E_{s2}) curves in Fig. 10, respectively. The central values of the E_{s1} and E_{s2} are 15 and 6 V/cm, respectively. Comparing the time-evolution curves, due to the deflection electric field at the entrance and exit of the spin filter, the decay of the metastable atom of case ② and ③ are more rapid than case ①. The adiabatic variation of $|b|^2$ with E_{rf} , as described in ref. [46], is clearly evident in the time-evolution curves. From the entrance to the exit of the spin filter, as E_{rf} increases gradually the deuterium atom will be a coherent mixture of α and β states, and then as E_{rf} slowly decreases to zero the α and β mixture is transformed back into a pure α state. There is a

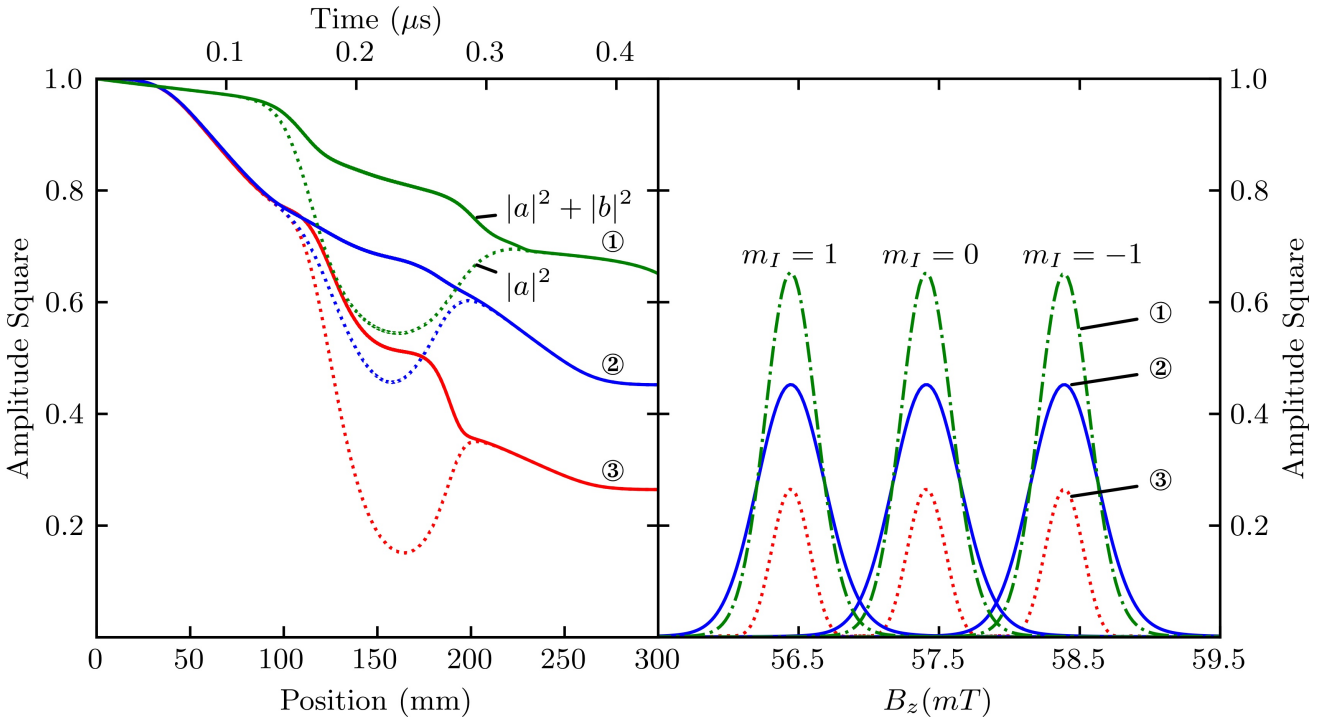


Fig. 11. Left plot shows the time-evolution of $|a|^2$ and $|a|^2 + |b|^2$, when a α -state deuterium atom with $m_I = 0$ going through the spin filter with a kinetic energy of 2.5 keV/u, for three different fields configurations. Right plot shows the variations of the transmission for metastable deuterium atom with different m_I in these three cases.

496 sever adiabatic loss for case ③. With the central value of E_s 521 atom with a moderate electric field can be approximated as,
 497 increasing from 6 to 15 V cm⁻¹, the adiabatic loss gradually
 498 diminishes, leading to an increase in the transmission. The
 499 calculated transmission of the metastable atom, represented
 500 as $|a|^2 + |b|^2$ at the exit of the spin filter, is a function of the
 501 B_s value. The value of B_s is swept from 55.5 to 59.5 mT,
 502 while maintaining its distribution as shown in Fig. 10. The
 503 variations of the transmission for metastable deuterium atom
 504 with different m_I in these three cases are illustrated in the
 505 right plot of Fig. 11, which also indicates the measurement
 506 spectra. Based on the calculated spectra, an increase in the
 507 central value of E_s leads to not only a higher transmission
 508 but also a spectrum with a larger width and a worse selec-
 509 tivity. Although the transmission in case ② is higher, it is
 510 unsuitable for separation of metastable deuterium atoms with
 511 different m_I due to the presence of overlapping between their
 512 resonant peaks. Case ②, however, is more favorable to be
 513 used for separation of metastable hydrogen atoms, because
 514 their two resonant peaks are more distant.

$$\tau = \left(\frac{19}{E} \right)^2 \times 10^{-6} \text{ s}, \quad (12)$$

522 where E is the magnitude of the electric field in V/cm [23].
 523 The kinetic energy of the atomic beam is 2.5 keV/u (7×10^7
 524 cm/s). In order to achieve a high detection efficiency for
 525 the metastable atoms at this energy, the first gap width and
 526 the electric field of the quenching lens are set to be 2 cm
 527 and 200 V/cm, respectively. Under these conditions, the life-
 528 time of the metastable atoms (9 ns) is much shorter than the
 529 drift time in the gap (30 ns), which ensures that all metastable
 530 atoms are quenched in the first gap. The window of the PMT
 531 is located 8 cm away from the beam axis and its effective
 532 diameter is 23 mm, which gives a geometric acceptance of
 533 0.5 %. The quantum efficiency of the photocathode (made
 534 of CsI) is considered to be 10 %. Overall, the detection effi-
 535 ciency for metastable atoms is about 0.05 %.

515

VI. DETECTION FOR METASTABLE ATOMS

537

VII. RESULTS AND DISCUSSION

516 As shown in Fig. 3, at the end the survival metastable atoms
 517 are quenched by the electric field of a quenching lens, and the
 518 emitted Lyman- α photons (121 nm) are registered by a PMT
 519 which is only sensitive to photons with wavelength of 110
 520 to 200 nm. The lifetime of metastable hydrogen (deuterium)

538 Based on the quantitative analyses for all of the critical pro-
 539 cesses of the LSP, the number of the Lyman- α photons de-
 540 tected at the quenching chamber can be calculated. A beam
 541 of protons (deuterons) with intensity of 1 mA, 6×10^{15} ions
 542 per second, gets into the ion beam transport line, because

543 of severe space charge effect, only 8% (4%) of the protons
 544 (deuterons) can be qualified to go through the downstream el-
 545 ements. At the sodium oven, 10% of the protons (deuterons)
 546 are converted to metastable atoms. Half of the metastable
 547 atoms stay in α states (the other half stay in β states), as there
 548 is no polarization at the sodium target. In addition, the frac-
 549 tions of the α states atoms with $m_I = \pm 1/2$ ($m_I = \pm 1, 0$)
 550 are 1/2 (1/3) under the assumption that the proton (deuteron)
 551 beam is unpolarized. After traversing the spin filter, 45%
 552 (25%) of the α state hydrogen (deuterium) atoms with the
 553 selected m_I retain in metastable state. Considering the de-
 554 tection efficiency of 0.05% for the metastable atoms at the
 555 quenching chamber, it is expected that the peak count rate of
 556 the PMT will be around 3×10^9 (5×10^8) photons per sec-
 557 ond. For each beam pulse lasting $100\mu s$, the number of the
 558 detected photons is 3×10^5 (5×10^4) per pulse. Consequently,
 559 a statistical error of about 0.4% will be obtained. To achieve
 560 a spectrum as depicted in the right plot of Fig. 11, it is nec-
 561 essary to ramp the magnetic field of the spin filter from 50
 562 to 65 mT in increments of 0.3 mT. The time allocated for
 563 each step should be 200 ms, ensuring that at least one beam
 564 pulse occurs during each step. This approach allows the entire
 565 spectrum to be recorded within a total duration of 10 s.

566 The background is considered to be dominated by colli-
 567 sions between the ground-state atoms produced by charge ex-
 568 change in the sodium oven and the residual gas [20]. The
 569 flux of the ground-state atoms obtained from the sodium
 570 oven is $N \approx 10^{14}$ atoms per second, which is three times
 571 that of the metastable atoms [37]. If the pressure in the
 572 quenching chamber is $p = 1 \times 10^{-6}$ mbar, times of the
 573 collisions in front of the PMT window can be calculated as
 574 $n = N \cdot \pi d^2 \cdot L \cdot p/kT \approx 2 \times 10^9$ collisions per second,
 575 where $d = 1 \times 10^{-10}$ m is the atom diameter, $L = 2$ cm is
 576 the length faced by the PMT window, $k = 1.38 \times 10^{-23}$ J/K
 577 is Boltzmann's constant, $T = 300$ K is the room tempera-
 578 ture. With the estimation that 10% of the collisions produce

579 110–200 nm photons and that 0.05% of them are detected by
 580 the PMT, the background count rate is about 10^5 s $^{-1}$ in the
 581 beam duration. The signal-to-background ratio is expected to
 582 be $10^3 \sim 10^4$.

583 Some corrections are necessary due to systematic factors,
 584 and the corrections depend on the properties of the compo-
 585 nents of the LSP. The corrections can be determined with the
 586 polarimeter itself. A systematic error of about 0.4% in the
 587 correction factors is reasonable [20]. Therefore, it is feasible
 588 to measure the pulsed polarized proton (deuteron) beam using
 589 the designed LSP with a precision of 1% in a few seconds.

590 VIII. SUMMARY

591 A Lamb-shift polarimeter tailored for the pulsed high-
 592 current polarized H^+/D^+ ion source is investigated system-
 593 atically in this study. Beam transport in the ion beam trans-
 594 port line engineered to match the polarized beam extracted
 595 from the ionizer with the LSP has been simulated and op-
 596 timized. The design of the sodium oven transforming pro-
 597 tons (deuterons) to be metastable atoms has been completed,
 598 whose operation status has been mastered by evaporation sim-
 599 ulation and thermal simulation. A spin filter has been de-
 600 signed, including a system of solenoidal windings with a ho-
 601 mogeneity better than 0.05% and a specific RF resonant cav-
 602 ity. Time-evolution of the wave function of the metastable
 603 hydrogen (deuterium) atoms in the spin filter has been calcu-
 604 lated with numerical integral. A metastable atom detection
 605 unit also has been designed. Based on these calculations, it is
 606 expected that the proton (deuteron) beam polarization can be
 607 measured with a precision of 1% within a few seconds with
 608 the designed LSP assembled directly downstream the polar-
 609 ized ion source.

610 [1] X. Cao, L. Chang, N.B. Chang, *et al.*, Electron ion col-
 611 linder in China. Nuclear Techniques **43**: 020001 (2020). doi:
 612 [10.11889/j.02533219.2020.hjs.43.020001](https://doi.org/10.11889/j.02533219.2020.hjs.43.020001)

613 [2] D. P. Anderle, V. Bertone, X. Cao, *et al.*, Electron-ion collider
 614 in China. Front. Phys. **16**: 64701 (2021). doi: [10.1007/s11467-021-1062-0](https://doi.org/10.1007/s11467-021-1062-0)

615 [3] J.C. Yang, J.W. Xia, G.Q. Xiao, *et al.*, High intensity heavy ion
 616 accelerator facility (HIAF) in China. Nucl. Instrum. Meth. B
 617 **317**: 263–265 (2013). doi: [10.1016/j.nimb.2013.08.046](https://doi.org/10.1016/j.nimb.2013.08.046)

618 [4] X.H. Zhou, J.C. Yang, the HIAF Project team, Status of the
 619 high-intensity heavy-ion accelerator facility in China. AAPPS
 620 Bull. **32**: 35 (2022). doi: [10.1007/s43673-022-00064-1](https://doi.org/10.1007/s43673-022-00064-1)

621 [5] R. Wang, X.R. Chen, The current status of electron ion collider
 622 in China. Few-body Syst. **63**: 48 (2022). doi: [10.1007/s00601-022-01751-3](https://doi.org/10.1007/s00601-022-01751-3)

623 [6] C.H. Zeng, T.B. Liu, P. Sun, *et al.*, Toward three-dimensional
 624 nucleon structures at the Electron-Ion Collider in China: A
 625 study of the Sivers function. Phys. Rev. D **106**: 094039 (2022).
 626 doi: [10.1103/PhysRevD.106.094039](https://doi.org/10.1103/PhysRevD.106.094039)

627 [7] Z. Ji, X.Y. Zhao, A.Q. GUO, *et al.*, Lambda polarization at
 628 Electron-ion collider in China. Nucl. Sci. Tech. **34**: 155 (2023).
 629 doi: [10.1007/s41365-023-01317-w](https://doi.org/10.1007/s41365-023-01317-w)

630 [8] M.X. Li, J.C. Yang, W.S. Wu, *et al.*, Maintaining polariza-
 631 tion with a constant field solenoid Siberian snake in the EicC-
 632 BRing. Nucl. Instrum. Meth. A **1031**: 166405 (2022). doi:
 633 [10.1016/j.nima.2022.166405](https://doi.org/10.1016/j.nima.2022.166405)

634 [9] A.S. Belov, Polarized ion sources: status and per-
 635 spective. Phys. Part. Nuclei **44**: 873 (2013). doi:
 636 [10.1134/S1063779613060038](https://doi.org/10.1134/S1063779613060038)

637 [10] A. Zelenski, Review of polarized ion source. Int. J.
 638 Mod. Phys.: Conference Series **40**: 1660100 (2016). doi:
 639 [10.1142/S2010194516601009](https://doi.org/10.1142/S2010194516601009)

640 [11] A.S. Belov, Production of polarized ions with nearly resonant
 641 charge-exchange collisions in plasma. AIP Conf. Proc. **980**:
 642 209 (2008). doi: [10.1063/1.2888089](https://doi.org/10.1063/1.2888089)

643 [12] R. Gebel, O. Felden, R. Maier, Polarized H^- and D^- beams
 644 at COSY/Jülich. AIP Conf. Proc. **980**: 231 (2008). doi:
 645 [10.1063/1.2888091](https://doi.org/10.1063/1.2888091)

648 [13] V.V. Fimushkin, *et al.*, in SPIN2018: The source of polarized
649 ions (SPI) and low energy polarimeter for the NUCLOTRON
650 facility, ed. by P. Lenisa, *et al.*. 23rd International Spin Physics
651 Symposium, Ferrara, Italy, September, 2018. (Sissa Medialab,
652 Trieste, Italy, 2019) doi: [10.22323/1.346.0114](https://doi.org/10.22323/1.346.0114)

653 [14] V.P. Derenchuk, A.S. Belov, Polarized D^- operation and de-
654 velopment of the IUCF ion source CIPIOS. AIP Conf. Proc.
655 **675**: 887 (2003). doi: [10.1016/j.nima.2023.168494](https://doi.org/10.1016/j.nima.2023.168494)

656 [15] A. zelenski, G. Atoian, E. Beebe, *et al.*, Optically pumped
657 polarized $^3He^{++}$ ion source development for RHIC/EIC.
658 Nucl. Instrum. Meth. A **1055**: 168494 (2023). doi:
659 [10.1016/j.nima.2023.168494](https://doi.org/10.1016/j.nima.2023.168494)

660 [16] A.S. Belov, S.K. Esin, L.P. Netchaeva, *et al.*, Polarized ions
661 from a storage cell. AIP Conf. Proc. **421**: 362 (1998). doi:
662 [10.1063/1.55006](https://doi.org/10.1063/1.55006)

663 [17] W. Haeberli, Source of polarized ions. Annu. Rev. Nucl. Sci.
664 **17**: 376 (1967). doi: [10.1146/annurev.ns.17.120167.002105](https://doi.org/10.1146/annurev.ns.17.120167.002105)

665 [18] R. Bieber, A. M. van den Berg, K. Ermisch, *et al.*, Performance
666 of the KVI in-beam polarimeter. Nucl. Instrum. Meth. A **457**:
667 12-21 (2001). doi: [10.1016/S0168-9002\(00\)00741-5](https://doi.org/10.1016/S0168-9002(00)00741-5)

668 [19] S.K. Lemieux, T.B. Clegg, H.J. Karwowski, *et al.*, A spin-
669 filter polarimeter for low energy hydrogen and deuterium ion
670 beams. Nucl. Instrum. Meth. A **333**: 434-442 (1993). doi:
671 [10.1016/0168-9002\(93\)91188-S](https://doi.org/10.1016/0168-9002(93)91188-S)

672 [20] R. Engels, R. Emmerich, J. Ley, *et al.*, Precision Lamb-shift
673 polarimeter for polarized atomic and ion beams. Rev. Sci. In-
674 strum. **74**: 4607-4615 (2003). doi: [10.1063/1.1619550](https://doi.org/10.1063/1.1619550)

675 [21] G.P. Lawrence, G.G. Ohlsen, J.L. McKibben, Source of polar-
676 ized negative hydrogen and deuterium Ions. Phys. Lett. B **28**:
677 594-596 (1969). doi: [10.1016/0370-2693\(69\)90195-6](https://doi.org/10.1016/0370-2693(69)90195-6)

678 [22] W.E. Lamb, R.C. Rutherford, Fine structure of the hydro-
679 gen Atom. Part II. Phys. Rev. **81**: 222-232 (1951). doi:
680 [10.1103/PhysRev.81.222](https://doi.org/10.1103/PhysRev.81.222)

681 [23] W.E. Lamb, R.C. Rutherford, Fine structure of the hydro-
682 gen atom. Part I. Phys. Rev. **79**: 549-572 (1950). doi:
683 [10.1103/PhysRev.79.549](https://doi.org/10.1103/PhysRev.79.549)

684 [24] H.R. Kremers, J.P.M. Beijers, N. Kalantar-Nayestanaki,
685 Design and performance of the Lamb-shift polarime-
686 ter. Nucl. Instrum. Meth. A **536**: 329-333 (2005). doi:
687 [10.1016/j.nima.2004.08.093](https://doi.org/10.1016/j.nima.2004.08.093)

688 [25] Simon J. Pütz, *et al.*, in PSTP2022: Polarization mea-
689 surement of a pulsed H^-/D^- ion Beam with a Lamb-shift
690 Polarimeter, ed. by Alexander Nass, *et al.*. 19th Workshop
691 on Polarized Sources, Targets and Polarimetry, Mainz, Ger-
692 many, August, 2022. (Sissa Medialab, Trieste, Italy, 2023)
693 [10.22323/1.433.0029](https://doi.org/10.22323/1.433.0029)

694 [26] S.X. Peng, *et al.*, in HB2016: Study on space charge com-
695 pensation of low energy high intensity ion beam in Peking Univer-
696 sity, ed. by Mohammad Eshraqi, *et al.*. 57th ICFA Advanced
697 Beam Dynamics Workshop on High-Intensity, High Bright-
698 ness and High Power Hadron Beams, Malmö, Sweden, 2016.
699 (JACoW, Geneva, Switzerland, 2016) doi:[10.18429/JACoW-HB2016-WEPM6Y01](https://doi.org/10.18429/JACoW-HB2016-WEPM6Y01)

700 [27] A.S. Belov, S.K. Esin, S.A. Kubalov, *et al.*, Pulsed high-
701 intensity source of polarized protons. Nucl. Instrum. Meth. A
702 **255**: 442-459 (1987). doi: [10.1016/0168-9002\(87\)91211-3](https://doi.org/10.1016/0168-9002(87)91211-3)

703 [28] D. Winklehner, Ion beam extraction from electron cyclotron
704 resonance ion source and the subsequent low energy beam
705 transport. Michigan State University, (2013).

706 [29] Z. Shen, Studies on ion beam extraction from high-intensity
707 highly charged ECR ion sources and the space charge effect,
708 Institute of Modern Physics, Chinese Academy of Sciences,
709 (2022).

710 [30] Y.G. Liu, Q. Wu, X. Zhang, *et al.*, Design of a 180° elec-
711 tromagnetic isotope separator with inhomogeneous magnetic
712 field. Nucl. Instrum. Meth. A **1006**: 165428 (2021). doi:
713 [10.1016/j.nima.2021.165428](https://doi.org/10.1016/j.nima.2021.165428)

714 [31] TraceWin, <https://www.dacm-logiciels.fr/tracewin>, 2024-10-
715 20.

716 [32] OPERA, <https://www.3ds.com/products/simulia/opera>, 2024-
717 10-20.

718 [33] T. Kalvas, O. Tarvainen, T. Ropponen, *et al.*, IBSIMU: A three-
719 dimensional simulation software for charged particle optics.
720 Rev. Sci. Instrum. **81**: 02B703 (2010). doi: [10.1063/1.3258608](https://doi.org/10.1063/1.3258608)

721 [34] T. Nagata, Charge changing collisions of atomic beams in
722 alkali-metal vapors. IV. Total cross sections for single-electron
723 capture by H^+ ion and H(1S) atom. J. Phys. Soc. Jpn. **48**:
724 2068-2075 (1980). doi: [10.1143/JPSJ.48.2068](https://doi.org/10.1143/JPSJ.48.2068)

725 [35] C.H. Liu, Y.Z. Qu, L. Liu, *et al.*, Charge transfer and excitation
726 in slow proton collisions with sodium. Phys. Rev. A **78**: 024703
727 (2008). doi: [10.1103/PhysRevA.78.024703](https://doi.org/10.1103/PhysRevA.78.024703)

728 [36] P. Pradel, F. Roussel, A.S. Schlachter, *et al.*, Formation of H
729 ($n = 2$) atoms by the nearly resonant process H^+ in Cs. multi-
730 ple collision processes. Phys. Rev. A **10**: 797-812 (1974). doi:
731 [10.1103/PhysRevA.10.797](https://doi.org/10.1103/PhysRevA.10.797)

732 [37] T. Nagata, Charge changing collisions of atomic beams in
733 alkali-metal vapors. III. Formations of H(2S) atoms from
734 H^+ ions. J. Phys. Soc. Jpn. **46**: 1622-1627 (1979). doi:
735 [10.1143/JPSJ.46.1622](https://doi.org/10.1143/JPSJ.46.1622)

736 [38] COMSOL, <https://cn.comsol.com/molecular-flow-module>,
737 2024-10-20.

738 [39] X.X. Lian, D.W. Zhong, Modeling and simulation of lithium
739 vacuum evaporation process using COMSOL Multiphysics. J.
740 Therm. Sci. **33**: 86-100 (2024). [10.1007/s11630-023-1914-8](https://doi.org/10.1007/s11630-023-1914-8)

741 [40] Y.C. Guo, Z.L. Su, Z.G. Li, *et al.*, Numerical investigation
742 on the startup performance of high-temperature heat pipes for
743 heat pipe cooled reactor application. Nucl. Sci. Tech. **32**: 104
744 (2021). [10.1007/s41365-021-00947-2](https://doi.org/10.1007/s41365-021-00947-2)

745 [41] R.W. Ditchburn, J.C. Gilmour, The vapor pressures of
746 monatomic vapors. Rev. Mod. Phys. **13**: 310-327 (1941). doi:
747 [10.1103/RevModPhys.13.310](https://doi.org/10.1103/RevModPhys.13.310)

748 [42] ANSYS, [https://www.ansys.com/zh-
749 cn/products/structures/ansys-mechanical#tab1-1](https://www.ansys.com/zh-cn/products/structures/ansys-mechanical#tab1-1), 2024-10-20.

750 [43] C.D. Roper, T.B. Clegg, A.J. Mendez, Electromagnetic field re-
751 quirements for a Lamb-shift spin-filter polarimeter. AIP Conf.
752 Proc. **343**: 132-136 (1995). doi: [10.1063/1.48843](https://doi.org/10.1063/1.48843)

753 [44] P.G. Sona, New method proposed to increase polarization in
754 polarized ion sources of H^- and D^- . Energ. Nucl. **14**: 295-
755 299 (1967).

756 [45] W.E. Lamb, R.C. Rutherford, Fine structure of the hydro-
757 gen atom. Part III. Phys. Rev. **85**: 259-276 (1952). doi:
758 [10.1103/PhysRev.85.259](https://doi.org/10.1103/PhysRev.85.259)

759 [46] G.G. Ohlsen, J.L. McKibben, Theory of a radio frequency spin
760 filter for a metastable hydrogen, deuterium, or tritium atomic
761 beam (No. LA-3725). Los Alamos National Lab.(LANL), Los
762 Alamos, NM (United States). (1967). doi: [10.2172/4517131](https://doi.org/10.2172/4517131)